Thermoelastic properties of bridgmanite using deep-potential molecular dynamics

Tianqi Wan [1,2] Chenxing Luo [1] Yang Sun [2,3,*] and Renata M. Wentzcovitch [1,4,5,6,7,†]

[1]*Department of Applied Physics and Applied Mathematics, Columbia University, New York, New York 10027, USA*
[2]*Department of Physics, Xiamen University, Xiamen 361005, China*
[3]*Department of Physics, Iowa State University, Ames, Iowa 50011, USA*
[4]*Department of Earth and Environmental Sciences, Columbia University, New York, New York 10027, USA*
[5]*Lamont–Doherty Earth Observatory, Columbia University, Palisades, New York 10964, USA*
[6]*Data Science Institute, Columbia University, New York, New York 10027, USA*
[7]*Center for Computational Quantum Physics, Flatiron Institute, New York, New York 10010, USA*

(Received 13 July 2023; revised 19 January 2024; accepted 23 January 2024; published 4 March 2024)

The high-pressure *Pbnm*-perovskite polymorph of $MgSiO_3$, i.e., bridgmanite (*Bm*), plays a crucial role in the Earth's lower mantle. It is likely responsible for ∼75 vol. % of this region and its properties dominate the properties of this region, especially its elastic properties that are challenging to measure at ambient conditions. This study combines deep-learning potential (DP) with density-functional theory (DFT) to investigate the structural and elastic properties of *Bm* under lower-mantle conditions. To simulate this system, we developed a series of potentials capable of faithfully reproducing DFT calculations using different functionals, i.e., local density approximation (LDA), Perdew-Burke-Ernzerhof parametrization (PBE), revised PBE for solids (PBEsol), and strongly constrained and appropriately normed (SCAN) meta–generalized-gradient approximation functionals. Our predictions with DP-SCAN exhibit a remarkable agreement with experimental measurements of high-temperature equations of states and elastic properties and highlight its superior performance, closely followed by DP-LDA in accurately predicting. This hybrid computational approach offers a solution to the accuracy-efficiency dilemma in obtaining precise elastic properties at high pressure and temperature conditions for minerals like *Bm*, opening a way to study the Earth material's thermodynamic properties and related phenomena.

DOI: 10.1103/PhysRevB.109.094101

I. INTRODUCTION

The Earth's lower mantle (LM), spanning from 670 to 2900 km in depth, constitutes approximately 56% of the Earth's total volume. It is the largest continuous region of the planet, experiencing a wide range of thermodynamic conditions from around 23 GPa and ∼1900 K to potentially 135 GPa and ∼4000 K [1]. The high-pressure *Pbnm*-perovskite polymorph of $MgSiO_3$, i.e., bridgmanite (*Bm*) [2], is the most abundant [3]. The physical properties of *Bm*, including its structural and elastic properties, are of paramount geophysical interest; they underpin the overall properties of the lower mantle. High-temperature elasticity is a fundamental property of solids in geophysics, as it can be used to determine the speeds of seismic waves.

To determine its pressure, volume, and temperature relationship, measurements of *Bm*'s structural properties under extreme conditions have extensively utilized x-ray diffraction on samples compressed in laser-heated diamond-anvil cells [4–6]. However, the full elastic tensor of *Bm* has only been determined experimentally at ambient conditions [4–6], because direct measurement of the elastic moduli at lower-mantle conditions poses significant challenges [7]. Extensive extrapolations encompassing the entire pressure-temperature (*P*-*T*) range relevant to the lower mantle (i.e., 23–135 GPa, ∼1900–4000 K) can introduce additional uncertainty due to different physical models.

Given that the extreme pressure and temperature conditions within the Earth's deep interior are challenging to reach experimentally, insights from *ab initio* based methods have become essential. *Ab initio* calculations have been extensively employed to verify and complement experimental studies of thermodynamic and elastic properties, phase stability, and effects of anharmonicity via the calculation of the phonon dispersion [8–16]. Alternatively, molecular dynamics (MD) addresses full anharmonic effects and has proved accurate in obtaining elastic properties at sufficiently high temperatures. However, such simulations faced limitations of system sizes and simulation timescales due to the expensive computational costs and poor scaling of purely *ab initio* calculations [17–19]. Moreover, classical MD critically depends on the precision of conventional empirical potentials in accurately representing interatomic interactions, i.e. the Born-Oppenheimer energy surface, across the extensive spectrum of pressures and temperatures encountered within the lower mantle. As previously reported, the utilization of strongly constrained and appropriately normed (SCAN) meta–generalized-gradient approximation (GGA) functional [20] can significantly

*yangsun@xmu.edu.cn
†rmw2150@columbia.edu

impact the equation of state (EOS), potentially leading to notable disparities, even in the determination of melting points compared to Perdew-Burke-Ernzerhof parametrization (PBE) [21]. However, due to the computational cost of SCAN being 2–5 times higher than that of PBE, SCAN remains infrequently employed in the field of geoscience.

Recently, machine-learning methods have presented a solution to the accuracy-efficiency dilemma [22–25] and have been successfully applied in MD simulations under extreme conditions. A few benchmarks have demonstrated that deep-learning potentials (DPs) [26] can achieve high accuracy in terms of force, energy, and the characterization of solid and liquid structures using hundreds to a few thousand reference configurations [27–29]. The combination of deep-learning potentials with advanced density functionals, such as SCAN, provides an opportunity to improve predictions of the EOS with respect to the traditional local density approximation (LDA) or GGA functionals and overcome its escalated computational costs [30].

In this study, we develop deep neural network potential models for *Bm* using density-functional theory (DFT) with various functionals. These potentials allow us to conduct extensive MD simulations covering a wide range of *P-T* conditions, enabling a detailed investigation of the compressional behavior, elastic moduli, and elastic anisotropy of *Bm* at high *P-T*s. We compare the potentials against pure DFT calculations and experimental measurements to evaluate their predictive power.

II. METHOD

A. DFT calculation

To generate the *ab initio* benchmark datasets for *Bm*, we performed *ab initio* MD (AIMD) simulations employing the Vienna *Ab initio* Simulation Package (VASP) [31]. We employed multiple exchange-correlation functionals to model the system, including the LDA [32], the Perdew-Burke-Ernzerhof parametrization (PBE) generalized gradient approximation [33], the revised PBE for solids (PBEsol) [34], and the SCAN functional [20]. The projector augmented-wave pseudopotential [35,36] was employed, along with a plane-wave cutoff energy of up to 550 eV. In AIMD simulations, we used 160-atom supercells of $MgSiO_3$ with $\Gamma(1 \times 1 \times 1)$ **k**-point mesh. The convergence criterion was set to 10^{-5}eV for the total energy. These DFT settings warranted good convergence of the calculated results [37].

B. Development of machine-learning potentials

Using the *ab initio* datasets of forces and energies, we developed DP models for *Bm* employing the DEEPMD-KIT package [38,39]. Two-body embedding with coordinates of the neighboring atoms (`se_e2_a`) was used for the descriptor. The embedding network was designed with a shape of (25, 50, 100), while the fitting network had a shape of (240, 240, 240). We used a cutoff radius of 6 Å and a smoothing parameter of 0.5 Å. The model was trained using the Adam optimizer [40] for 1×10^6 training steps, with the learning rate exponentially decaying from 1×10^{-3} to 3.51×10^{-8} during the training process. The loss function $\mathcal{L}(p_e,\ p_f)$ is given by [38]

$$\mathcal{L}(p_e,\ p_f) = p_e|\Delta e|^2 + \frac{p_f}{3N}|\Delta f_i|^2, \tag{1}$$

where p_e linearly decays from 1.00 to 0.02, while p_f linearly increases from 1×10^0 to 1×10^3 throughout the training process.

We employed the DP-GEN concurrent learning scheme to create the reference dataset and generate the potential [41]. The training of our potential was executed using a customized workflow implemented in SNAKEMAKE [42], which incorporates the DP-GEN scheme. Outsourcing the workflow logic to SNAKEMAKE enables paralleled file generation and enforces a clear specification of input–output and their transformations in each step. Emphasizing modularization for ease of maintenance and customization, our approach utilized JINJA, a templating language, for text-input file generation. This facilitated seamless integration with various software, separated the main workflow logic from structure manipulation code, and resulted in simplified testing with an impressive 80% unit-test coverage. Consequently, we achieved a much leaner architecture and codebase, reducing the lines of code from over 10 000 in the original DP-GEN implementation to less than 1000 in the current implementation. The improved robustness allowed for easy adaptation of DP-GEN to complex HPC environments. Initially, we randomly extracted 100 labeled configurations from 25 MD runs spanning various *P-T* ranges, covering 0–160 GPa and 300–4000 K to generate the initial potentials, shown in Fig. S1 (see Supplemental Material [43]). We performed four DP-GEN iterations to explore the configuration space and ultimately achieve a potential that meets the desired accuracy for MD simulations. We trained four candidate DPs initialized with different random seeds in each iteration. The error estimator (model deviation) ϵ_t is determined based on the force disagreement between the candidate DPs [41,44]. The expression for ϵ_t is

$$\epsilon_t = \max_i \sqrt{\langle \|F_{\omega,i}(\mathcal{R}_t) - \langle F_{\omega,i}(\mathcal{R}_t)\rangle\|^2\rangle},$$

where $F_{\omega,i}(\mathcal{R}_t)$ represents the force on the ith atom predicted by the ωth potential for the configuration $\mathcal{R}_t$. After the DP-GEN iterations, the final training dataset comprises 3000 configurations annotated with *ab initio* force and energy information. We trained four potentials to reproduce the results of four exchange-correlation functionals: LDA, PBE, PBEsol, and SCAN. Consequently, we generated DP-LDA, DP-PBE, DP-PBEsol, and DP-SCAN potentials.

We used the LAMMPS package [45] to perform MD simulations. The Nosé-Hoover thermostat [46,47] was employed in the *NVT* ensemble simulation. In the elastic calculations, the strain value is chosen as ±1%. We employed a 250-ps equilibration period with a time step of 0.5 fs, followed by a total simulation time of 900 ps to compute a total of 12 elastic modulus parameters. We obtained phonon dispersions using the finite-displacement method implemented in PHONOPY [48] and PHONOLAMMPS codes [49] using a supercell of $2 \times 2 \times 2$ with 160 atoms. The elastic properties were determined with DPMD using stress-strain relation [50–52] with 1280 atoms and infinitesimal deformation.

C. Elastic anisotropy calculations

We utilized the Christoffel equation [53]:

$$[\mathbf{G} - \rho v^2 \mathbf{I}]\mathbf{a} = 0,$$

to determine wave velocities along any direction. Here, $\mathbf{G}$ represents the Christoffel matrix $G_{ij} = \boldsymbol{c}_{ijkl} n_j n_l$, where $\boldsymbol{c}_{ijkl}$ is the stiffness tensor, and n_j and n_l are, respectively, the normalized wave-vector components in the j and l directions: $\mathbf{n} = \mathbf{k}/|\mathbf{k}|$. Here, v denotes the phase velocity of a given wave mode for the given propagation direction ($\mathbf{n}$), and $\mathbf{a}$ denotes the corresponding polarization vector. For a given density, stiffness tensor, and propagation direction, the Christoffel matrix $\mathbf{G}$ possesses three eigenvalues and three corresponding eigenvectors. These eigenvectors signify the polarization vectors of the three wave modes (P and two S), with the corresponding eigenvalues indicating the squared phase velocities v^2 of the waves.

For a more intuitive exploration of *Bm*'s anisotropy, the azimuthal anisotropy for compressional (A_P) and shear (A_S) waves is quantified by the following relations:

$$A_P = \frac{V_{P\max} - V_{P\min}}{\langle V_P \rangle} \times 100,$$

$$A_S = \frac{V_{S\max} - V_{S\min}}{\langle V_S \rangle} \times 100,$$

where $\langle V_P \rangle$ and $\langle V_S \rangle$ are the isotropic aggregate velocities.

III. RESULTS

A. Validation of machine-learning potential

We commence by evaluating the precision of our machine-learning potential through an extensive comparison with DFT calculations, encompassing energies, atomic forces, and stresses. We have quantified the root-mean-square error (RMSE) to gauge the accuracy of the DP's predictions on the validation sets. As illustrated in Fig. 1, our calculations employing different functionals yield RMSE values of approximately 0.9 meV/atom, 0.068 eV/Å, and 0.45 GPa for potential energies, atomic forces, and stresses, respectively. All these potentials show small RMSE compared to the DFT data, indicating the present deep potentials are well trained. Also, as shown in Table S1 [43], our potential exhibits superior precision in describing energy compared to other machine-learning potentials [54,55]. This enhanced accuracy contributes to the reliability of our EOS predictions.

Figure 2 shows the radial distribution functions of *Bm* at 4000 K and 120 GPa, obtained from both DFT-LDA and DP-LDA simulations. The DPs faithfully reproduce the $g(r)$ data derived from DFT calculations, indicating the DP's capability to capture *Bm*'s structural and bonding properties accurately.

Since phonon dispersions are crucial in determining high-temperature properties, we also compare in Fig. 3 these dispersions at 0 GPa obtained with DP-LDA and DFT-LDA calculations. We see excellent agreement across almost all phonon branches, with only minor deviations in a few high-frequency optical branches along the $\Gamma - Z$ path. The agreement between DPMD and DFT predictions, encompassing force, potential energy, $g(r)$, and phonon dispersion, attests to the robustness of our DP. Therefore, we can confidently proceed and compute the EOS and elastic coefficients, $\boldsymbol{c}_{ij}$, at high-pressure and high-temperature conditions.

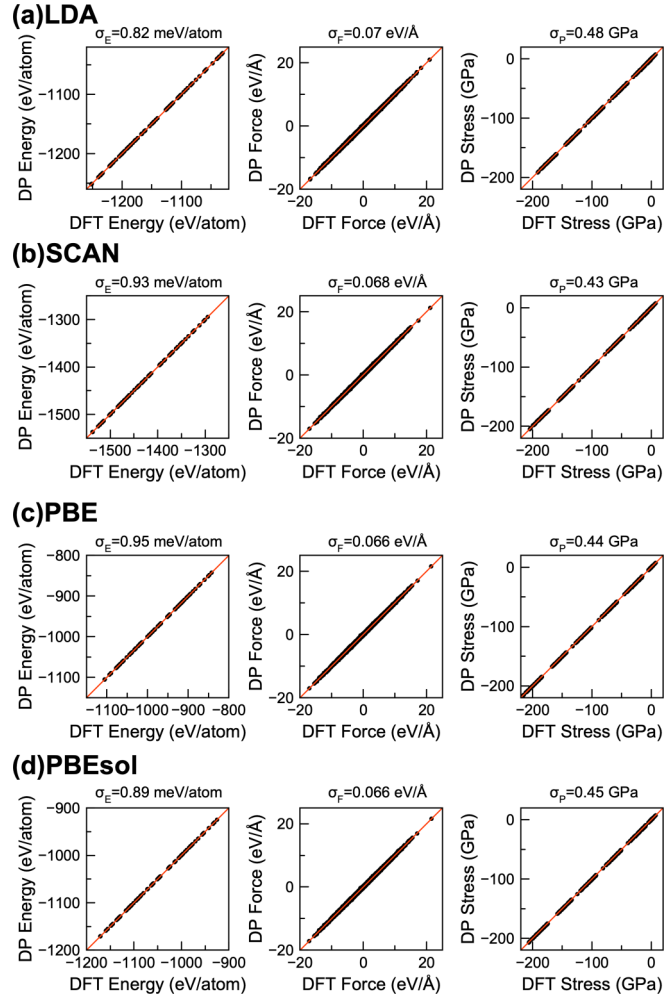

FIG. 1. Comparison of DP and *ab initio* calculations on the potential energy, atomic forces, and stresses with (a) LDA, (b) SCAN, (c) PBE, and (d) PBEsol for all the test data which covers 0–160 GPa and 300–4000 K.

B. Equation of state

We compute the EOS across a broad range of P-T conditions. Figure 4 compares EOSs obtained from our DP and previous LDA calculations [37]. Notably, the third-order Birch-Murnaghan EOS derived from DPMD results agrees exceedingly well with the DFT calculations. However, it is worth noting that both DP-LDA and DFT calculations tend to underestimate the pressure at a given volume when compared to experimental values [56–65]. This discrepancy can be attributed mainly to the LDA functional employed in the present calculations. We also note that the DP calculations are based on classical MD simulations without taking into account the quantum effect of zero-point motion (ZPM). This ZPM effect was included in the previous LDA calculation [37], which manifests in the slight underestimation of DP-300 K compared with the DFT-300 K results. This ZPM effect is clearly reduced at 2000 K as the system approaches the classical

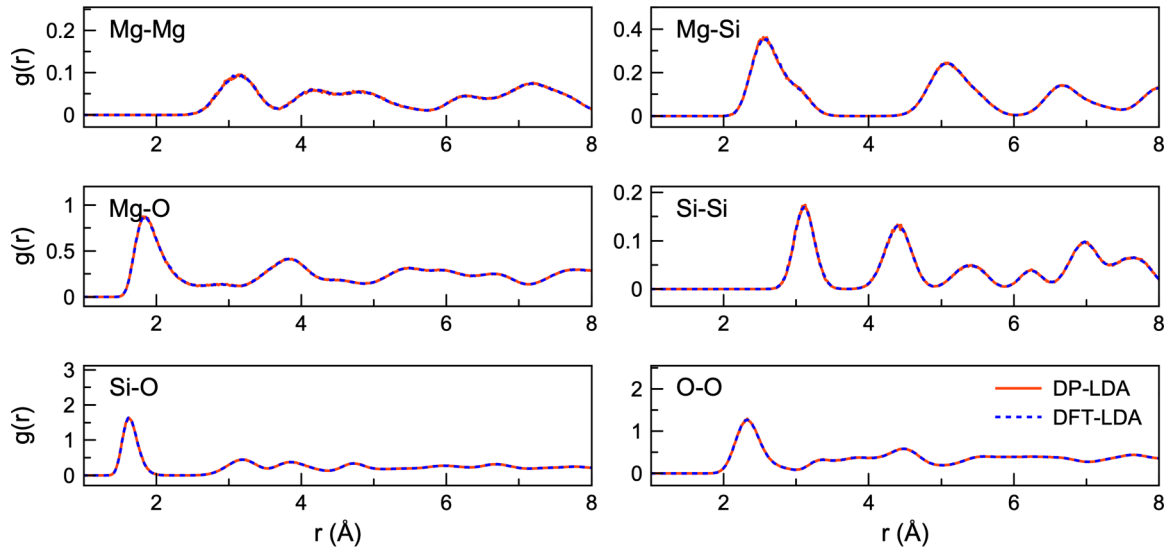

FIG. 2. Radial distribution functions of *Bm* at 4000 K and 120 GPa from DFT-LDA calculations (dotted blue lines) and DP-LDA (solid red lines).

limit. Figure 4 also compares the EOS obtained with various functionals and experimental data at 300 and 2000 K. The commonly used DP-PBE and DP-PBEsol functionals tend to overestimate the volume; DP-LDA slightly underestimates it, while DP-SCAN performs significantly better. For instance, at 2000 K, with experimental data as a reference, the RMSE for DFT-LDA, DP-LDA, and DP-SCAN are 4.95, 4.62, and 3.68 $Å^3$ per atom, respectively. It is evident that DP-SCAN provides the most accurate description of the EOS. Considering the crucial significance of EOS accuracy for elastic properties, the accuracy of DP-SCAN's EOS greatly favors the use of DP-SCAN in subsequent calculations of elastic properties.

C. Thermoelasticity

In Fig. 5, we present a comparative analysis of elastic coefficients obtained through DPMD and those derived from prior calculations involving PBE-GGA [17,66], LDA calculations [10], along with experimental measurement [4–6]. We have chosen the experimental data reported by Sinogeikin *et al.* [5] as our reference dataset, and a comprehensive compilation of these coefficients is provided in Table S2 [43]. One

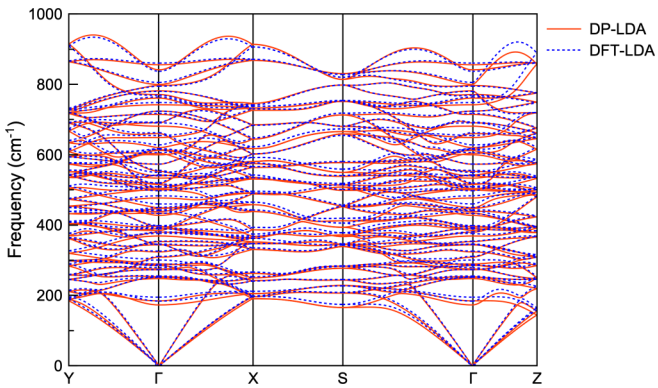

FIG. 3. Phonon dispersions of *Bm* at 0 GPa calculated by DFT-LDA (dotted blue lines) and DP-LDA (solid red lines).

can see DP-SCAN yields results most consistent with measurements when compared to the other calculations, with the lowest RMSE = 7.36 GPa. Furthermore, DP-SCAN consistently achieves discrepancies within 6% for all elastic tensor components, $\boldsymbol{c}_{ij}$, when compared to experimental data, a level of accuracy that surpasses other computational approaches. This underscores DP-SCAN's superior predictive capability for elastic properties. DP-LDA also agrees well with the experimental data, with minor discrepancies observed in $\boldsymbol{c}_{44}$ and $\boldsymbol{c}_{55}$. The DP-PBE and DP-PBEsol methods do not perform equally well to describe the elastic properties calculations. Their deviation from the experimental data is larger than 10%. It is noteworthy that previous DFT [66] calculations also yield good elastic properties at room temperature. This accuracy can be attributed to their approach of deriving results from acoustic phonon dispersions, bypassing numerical challenges arising from finite grid sampling in reciprocal space and a limited number of plane waves. However, it should be noted that their calculations exhibited a significant 13% deviation from experimental values for $\boldsymbol{c}_{12}$, highlighting the overall superior performance of our DP-SCAN results. The present study with DP calculations enables large-scale MD simulations to directly investigate the stress-strain relationship and obtain accurate elastic behavior, which should ensure the reliability and robustness of our results.

Figure 6 illustrates the influence of pressure (P) and temperature (T) on the elastic coefficients, revealing a nearly linear rise with increasing P and a linear decline with increasing T. These findings align with earlier measurements [4,6] conducted at 300 K. Notably, both the DP-SCAN and DP-LDA functionals exhibit very good agreement with experimental data at 0 GPa. However, DP-SCAN results agree better with measurements [6] at high pressure, e.g., up to 80 GPa. Remarkably, our DP-SCAN results also exhibit better alignment with experiments than prior DFT calculations at 300 K for elevated pressures, especially for $\boldsymbol{c}_{12}$, $\boldsymbol{c}_{13}$, and $\boldsymbol{c}_{66}$ [19]. At temperatures ranging from 1500 to 2500 K, as depicted in Fig. 7, the disparities between DP-SCAN and

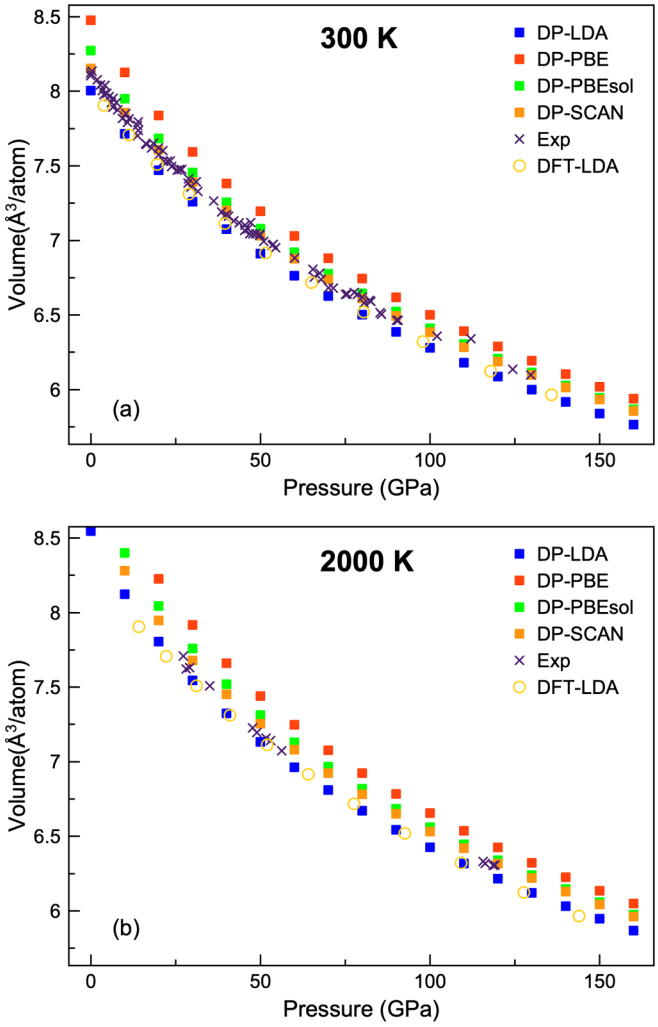

FIG. 4. Equation of state of *Bm* at (a) 300 K and (b) 2000 K. Results from DP-LDA, DP-PBE, DP-PBEsol, and DP-SCAN correspond with blue, red, green, and orange squares, respectively. Experimental data shown as crosses are from Refs. [56–65]. DFT calculations shown as circles are from Ref. [37].

prior computations remain within an acceptable margin. However, as the temperature soars to 3500 K, these distinctions become increasingly pronounced, notably for c_{44}, c_{55}, and

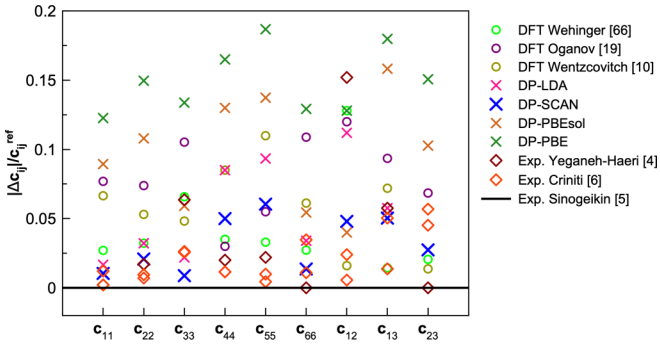

FIG. 5. Relative difference of elastic moduli of *Bm* at 300 K and 0 GPa. Experimental values are from Refs. [4–6]. Circles are from previous GGA calculations [19,66] and previous LDA calculations [10]. Crosses are our DP results with different functionals.

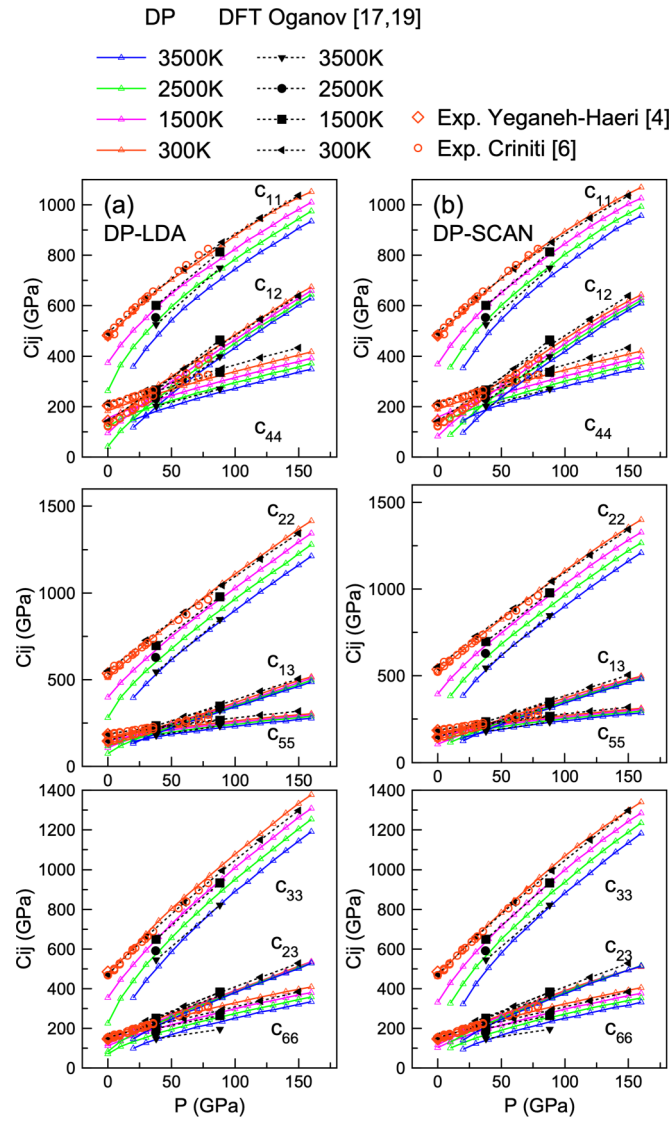

FIG. 6. Pressure dependence of the isothermal elastic constants of *Bm* with (a) DP-LDA and (b) DP-SCAN. Solid lines correspond to our DP results. Open diamonds and open circles represent measurements [4,6]. Solid symbols are results of previous calculations [17,19]. Symbol colors denote temperatures.

c_{66}, exhibiting deviations of up to 17%. It is noteworthy that our calculations not only demonstrate superior agreement with experimental data at 300 K and improved EOS behavior at 2000 K but also comprehensively address anharmonic effects while surmounting limitations in simulation size. Consequently, our DP-SCAN results should be more reliable. In principle, it requires high *P-T* experimental data to validate these predictions, but such measurements are unavailable. We note that the comparison with experimental data is based on the isothermal elastic coefficients, as the difference between isothermal and adiabatic elastic coefficients is relatively small. The inclusion of adiabatic correction may increase the nonshear elastic coefficients very little [14,67,68].

Figure 8 illustrates the pressure-temperature dependence of the Voigt-Reuss-Hill–averaged [69,70] bulk modulus (K_T), shear modulus (G), as well as the compressive (V_P) and

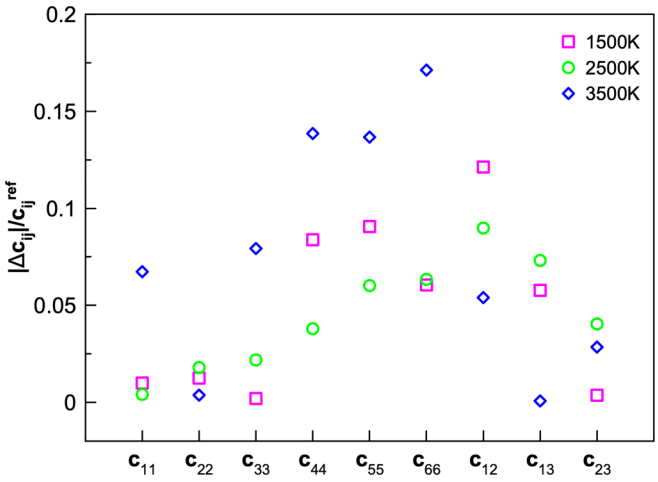

FIG. 7. Relative difference of $\boldsymbol{c}_{ij}$ at 40 GPa between DP-SCAN and previous calculations [17] with DP-SCAN as the reference. Symbols denote different temperatures.

shear (V_S) wave velocities from DP-LDA and DP-SCAN. These properties are derived from the elastic coefficients ($\boldsymbol{c}_{ij}$) and exhibit a consistently positive pressure dependence and negative temperature dependence. In Figs. 8(a) and 8(b), we compare the predicted velocities and density of *Bm* with previous measurements [4–6] and seismological values of the Preliminary Reference Earth Model (PREM) [71]. The density (ρ) exhibits relatively low sensitivity to temperature variations, with only a 1% change observed under a 1000 K fluctuation at conditions representative of the lower mantle's depths. At room temperature, longitudinal wave velocities (V_P) derived from both DP-LDA and DP-SCAN are in good agreement with experimental measurements. However, DP-SCAN outperforms DP-LDA on shear-wave velocity (V_S) predictions at higher pressures. Both V_S^{PREM} and V_P^{PREM} closely match the 2500 to 3500 K isothermal shear- and compressive-wave velocities, in the mantle. Moreover, V_P^{PREM} intersects two V_P isotherms, at 2500 and 3500 K, suggesting a temperature difference of less than 1000 K from top to bottom in the lower mantle if it were entirely composed of *Bm*. Considering the shear and bulk moduli depicted in Figs. 8(c) and 8(d), our results agree well with experimental data at 300 K. Both K^{PREM} and G^{PREM} closely follow the corresponding 2500 K isotherms. Also, our shear modulus displays favorable agreement with previous DFT calculations [17], even at higher temperatures. However, some minor discrepancies are observed in the bulk modulus compared to previous DFT calculations. Considering the overlap between the K_T curve of previous DFT calculations at 1500 K and that of experimental data at 300 K, our calculations exhibit a notably better agreement. This also reaffirms the accuracy of our prior $\boldsymbol{c}_{ij}$ calculations. In summary, it becomes evident that DP-SCAN emerges as a most promising potential for accurately describing these properties and should become the standard.

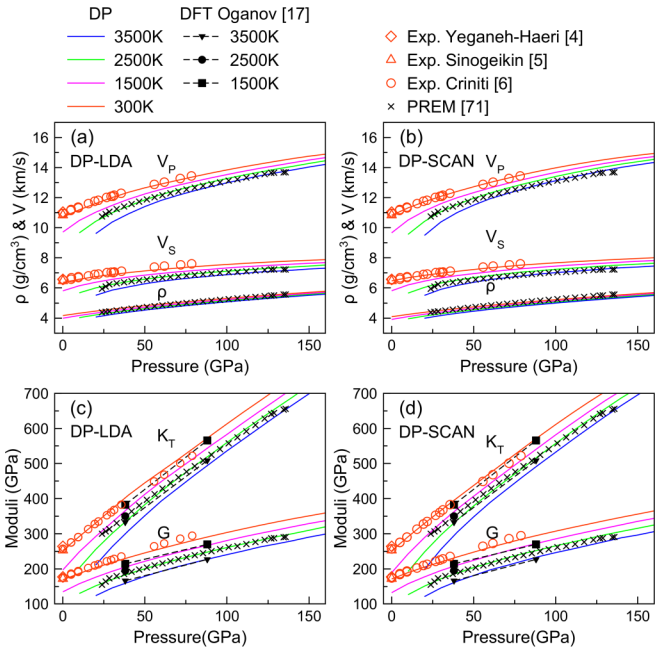

FIG. 8. Pressure dependence of density (ρ), isotropic longitudinal ($V_P = \sqrt{(K_T + 4G/3)/\rho}$), and shear- ($V_S = \sqrt{G/\rho}$) wave velocities, isothermal bulk moduli (K_T), and shear (G) moduli of *Bm*. Solid lines in (a) and (c) are our DP-LDA results, while solid lines in (b) and (d) are our DP-SCAN results. Triangles and circles are the experimental results [4–6]. Symbols connected by squares are the results of previous calculations [17]. Colors denote temperatures. Black crosses are PREM data [71].

D. Elastic anisotropy

Understanding the elastic anisotropy of *Bm*, particularly its intricate pressure and temperature dependencies, is crucial for deciphering seismological observations and extracting insights from mantle-flow geometry. Based on our DP-SCAN, we compute the elastic anisotropy of *Bm* with the Christoffel equation [53] and determine the single-crystal elastic-wave velocities in diverse directions. Illustrated in Fig. 9(a), our calculation demonstrates a good agreement of wave velocities in *Bm* with experimental values reported at ambient conditions [5,6]. Elastic-wave velocities exhibit substantial variations with both propagation and polarization directions, suggesting that the *Bm* exhibits strong anisotropy in both compressional (P) and shear (S) wave velocities [6]. This anisotropy depends on pressure and temperature in a complicated manner. Thus, we performed interpolation for each elastic coefficient ($\boldsymbol{c}_{ij}$) with respect to both pressure and temperature to compute the anisotropy map, as presented in Figs. 9(b)–9(f).

In Fig. 9(b), A_P initially decreases and then increases with rising pressure, aligning with previous calculations [72]. We note a shift in the turning point towards higher pressures with increasing temperature. In the temperature range of 300 to 3500 K, the variation in A_P remains below 4% at constant pressure, with low sensitivity to temperature changes. As shown in Fig. 9(c), A_S initially decreases and then increases with rising pressure, with the turning point shifting to higher values as temperature increases, similar to the behavior observed in A_P. Even though A_S and A_P share similarities, the azimuthal anisotropy of shear waves is markedly stronger than that of compressional waves. Importantly, A_S is significantly larger at higher temperatures, showcasing heightened sensitivity to temperature changes at lower pressures. The difference

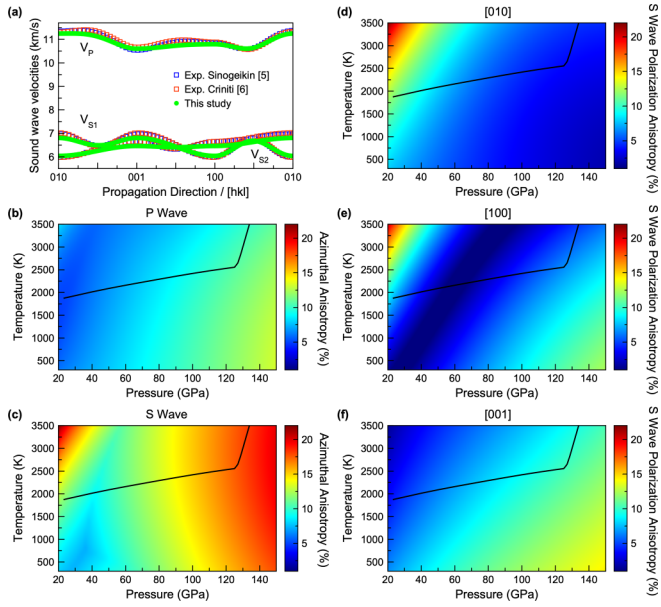

FIG. 9. (a) Variation of compressional and shear-wave velocities of *Bm* with different propagation direction at ambient condition. Blue and red open squares are experimental data from Refs. [5,6]. Pressure and temperature dependence of azimuthal anisotropy for (b) *P* wave and (c) *S* wave, alongside pressure and temperature variation of polarization anisotropy for (d) [010], (e) [100], and (f) [001] directions. The black lines indicate the geotherm of the lower mantle [73,74].

in A_S between 300 and 3500 K ranges from 14% at 20 GPa to 2% at 150 GPa.

The two shear waves propagate with distinct velocities, leading to *S*-wave birefringence. Figures 9(d)–9(f) show the pressure and temperature dependence of polarization anisotropy in shear waves for three crystallographic directions, [010], [100], and [001], respectively. For the [010] direction, anisotropy decreases with increasing pressure but rises with higher temperatures. This increase, however, diminishes at higher pressures. At 20 GPa, anisotropy for the [010] direction increases from 7.97% at 300 K to 21.85% at 3500 K, compared to a modest increase from 1.96 to 4.44% at 150 GPa. For the [100] direction, the anisotropy exhibits an initial decrease followed by an increase as pressure rises with the turning point shifting towards higher pressures as temperature increases. Similar trends hold for temperature variations; the anisotropy initially decreases with rising temperature before transitioning to an increase, and the turning point amplifying at higher pressures. The [001] direction presents a simpler scenario, with monotonic pressure and temperature dependencies of anisotropy. Anisotropy in the [001] direction increases with rising pressure but decreases with increasing temperature. Our findings indicate that *Bm* exhibits significant anisotropy, introducing a complex interplay of pressure and temperature on seismic anisotropy. Surprisingly, many seismological investigations [71,72] of the lower mantle have not unveiled such pronounced anisotropy, suggesting a potential cause in the random orientation of *Bm* grains. Consequently, the discerned anisotropy patterns in *Bm* provide valuable insights into the underlying mechanisms influencing mineral deformation and structural preferences within the lower mantle.

IV. DISCUSSION

Our study highlights the accuracy of a hybrid approach that combines DFT with DP to investigate the equation of state and elastic properties of *Bm* at high *PT* conditions. The DP-GEN active-learning scheme utilized to develop the potential demonstrates high efficiency, requiring only a few thousand reference DFT calculations completed within a few days. The computational cost of our DFT calculations is even lower than that of a typical AIMD run required for sampling a single (P, T) point. The resulting potential reproduces DFT results with excellent fidelity. This enhanced efficiency enables us to utilize more accurate functionals and conduct simulations on complex systems with improved accuracy in larger and more complex systems, longer timescales, and denser (P, T) sampling that were unattainable with pure DFT calculations.

In previous investigations, the DPs were developed to explore lattice thermal conductivity and melting behavior for the *Bm* [54,55]. Our work distinguishes itself by using the DP-GEN concurrent learning scheme, which deviates from the iterative learning scheme utilized by Deng [54], and employing a customized workflow implemented in SNAKEMAKE, which may contribute to the superior precision of our potential in characterizing energy. Furthermore, it is noteworthy that Deng [54] utilized the PBE functional, while Yang [55] employed the PBEsol functional for *Bm*. While they could capture thermal conductivity and melting behavior within their respective studies, our results suggest that the SCAN functional performs the best in calculations of the EOS and elastic properties of *Bm* while PBE or PBEsol should be avoided. These results underscore the crucial importance of employing the most predictive functionals to accurately determine the thermodynamic properties of materials while emphasizing the potential for future high *P*-*T* research applications.

The hybrid DFT-based machine-learning approach transforms how we approach systems at extreme conditions with computational methods. It enables more accurate predictions for increasingly complex systems. Such an efficient and accurate approach for simulating the elastic properties of LM minerals at high *P*-*T* conditions is poised to contribute to a deeper understanding of processes shaping the Earth's internal state.

V. CONCLUSION

Our study focuses on developing and testing deep-learning potentials using different DFT functionals to investigate the EOS and thermoelasticity of *Bm* under high-pressure and high-temperature conditions in the lower mantle. Our results demonstrate the accuracy of the DP approach by successfully reproducing radial distributions and phonon dispersions, with RMSEs of 0.8 meV per atom for energy and 0.07 eV/Å for atomic forces, further validating the robustness of our DP results. Regarding the EOS, we find that the choice of exchange-correlation functional in DFT calculations significantly impacts accuracy. DP-LDA slightly underestimates pressure at a given volume, while DP-PBE and DP-PBEsol

overestimate it, even in the absence of ZPM effects. In contrast, the DP-SCAN method exhibits outstanding agreement with experimental data, demonstrating its superior capability for EOS prediction. We also establish the consistency of the elastic properties predicted by DP-SCAN and DP-LDA with previous quasiharmonic LDA calculations at high temperatures, confirming insignificant anharmonic effects on the high-temperature properties of *Bm*. Additionally, mantle properties reported by the PREM fall in the range of *Bm* properties expected at lower-mantle temperatures. Last, our calculations not only closely match the experimentally observed anisotropy at ambient conditions but also reveal the intricate interplay between pressure and temperature influencing the anisotropy of *Bm* at lower-mantle conditions. We demonstrate that the synergistic application of DP and DFT provides a powerful means to predict EOS and elastic properties of mantle minerals more accurately at relevant temperatures, a task that has presented substantial experimental challenges.

ACKNOWLEDGMENTS

T.W. and Y.S. acknowledge support from the National Natural Science Foundation of China (Grant No. 42374108) and the Fundamental Research Funds for the Central Universities (Grant No. 20720230014). Work at Columbia University was supported by the National Science Foundation Award No. EAR-1918126. C.L. acknowledges support from the DOE Award No. DE-SC0019759. This work used Bridges-2 system at Pittsburgh Supercomputing Center, the Anvil system at Purdue University, the Expanse system at San Diego Supercomputing Center, and the Delta system at National Center for Supercomputing Applications from the Advanced Cyberinfrastructure Coordination Ecosystem: Services & Support (ACCESS) program, which is supported by National Science Foundation Grants No. 2138259, No. 2138286, No. 2138307, No. 2137603, and No. 2138296. S. Fang and T. Wu from Information and Network Center of Xiamen University are acknowledged for their help with the GPU computing.

[1] A. Zerr, A. Diegeler, and R. Boehler, Solidus of Earth's deep mantle, Science **281**, 243 (1998).

[2] L. Liu, Silicate perovskite from phase transformations of pyrope-garnet at high pressure and temperature, Geophys. Res. Lett. **1**, 277 (1974).

[3] E. Knittle and R. Jeanloz, Synthesis and equation of state of (Mg,Fe) SiO_3 perovskite to over 100 gigapascals, Science **235**, 668 (1987).

[4] A. Yeganeh-Haeri, Synthesis and re-investigation of the elastic properties of single-crystal magnesium silicate perovskite, Phys. Earth Planet. Inter. **87**, 111 (1994).

[5] S. V. Sinogeikin, J. Zhang, and J. D. Bass, Elasticity of single crystal and polycrystalline $MgSiO_3$ perovskite by Brillouin spectroscopy, Geophys. Res. Lett. **31**, L06620 (2004).

[6] G. Criniti, A. Kurnosov, T. Boffa Ballaran, and D. J. Frost, Single-crystal elasticity of $MgSiO_3$ bridgmanite to mid-lower mantle pressure, J. Geophys. Res. Solid Earth **126**, e2020JB020967 (2021).

[7] J. F. Lin, Z. Mao, J. Yang, and S. Fu, Elasticity of lower-mantle bridgmanite, Nature (London) **564**, E18 (2018).

[8] K. Parlinski and Y. Kawazoe, Ab initio study of phonons and structural stabilities of the perovskite-type $MgSiO_3$, Eur. Phys. J. B **16**, 49 (2000).

[9] B. B. Karki, R. M. Wentzcovitch, S. De Gironcoli, and S. Baroni, Ab initio lattice dynamics of $MgSiO_3$ perovskite at high pressure, Phys. Rev. B **62**, 14750 (2000).

[10] R. M. Wentzcovitch, B. B. Karki, M. Cococcioni, and S. de Gironcoli, Thermoelastic properties of $MgSiO_3$ perovskite: Insights on the nature of the Earth's lower mantle, Phys. Rev. Lett. **92**, 018501 (2004).

[11] A. R. Oganov and G. D. Price, Ab initio thermodynamics of $MgSiO_3$ perovskite at high pressures and temperatures, J. Chem. Phys. **122**, 124501 (2005).

[12] P. Carrier, R. Wentzcovitch, and J. Tsuchiya, First-principles prediction of crystal structures at high temperatures using the quasiharmonic approximation, Phys. Rev. B **76**, 064116 (2007).

[13] D. B. Zhang, T. Sun, and R. M. Wentzcovitch, Phonon quasiparticles and anharmonic free energy in complex systems, Phys. Rev. Lett. **112**, 058501 (2014).

[14] C. Luo, X. Deng, W. Wang, G. Shukla, Z. Wu, and R. M. Wentzcovitch, cij: A Python code for quasiharmonic thermoelasticity, Comput. Phys. Commun. **267**, 108067 (2021).

[15] G. Shukla, Z. Wu, H. Hsu, A. Floris, M. Cococcioni, and R. M. Wentzcovitch, Thermoelasticity of Fe^{2+}-bearing bridgmanite, Geophys. Res. Lett. **42**, 1741 (2015).

[16] G. Shukla, M. Cococcioni, and R. M. Wentzcovitch, Thermoelasticity of Fe^{3+}- and Al-bearing bridgmanite: Effects of iron spin crossover, Geophys. Res. Lett. **43**, 5661 (2016).

[17] A. R. Oganov, J. P. Brodholt, and G. D. Price, The elastic constants of $MgSiO_3$ perovskite at pressures and temperatures of the earth's mantle, Nature (London) **411**, 934 (2001).

[18] F. C. Marton and R. E. Cohen, Constraints on lower mantle composition from molecular dynamics simulations of $MgSiO_3$ perovskite, Phys. Earth Planet. Inter. **134**, 239 (2002).

[19] A. R. Oganov, J. P. Brodholt, and G. D. Price, Ab initio elasticity and thermal equation of state of $MgSiO_3$ perovskite, Earth Planet. Sci. Lett. **184**, 555 (2001).

[20] J. Sun, A. Ruzsinszky, and J. Perdew, Strongly constrained and appropriately normed semilocal density functional, Phys. Rev. Lett. **115**, 036402 (2015).

[21] M. Rang and G. Kresse, First-principles study of the melting temperature of MgO, Phys. Rev. B **99**, 184103 (2019).

[22] Y. Ouyang, Z. Zhang, C. Yu, J. He, G. Yan, and J. Chen, Accuracy of machine learning potential for predictions of multiple-target physical properties, Chin. Phys. Lett. **37**, 126301 (2020).

[23] Q. Zeng, B. Chen, X. Yu, S. Zhang, D. Kang, H. Wang, and J. Dai, Towards large-scale and spatiotemporally resolved diagnosis of electronic density of states by deep learning, Phys. Rev. B **105**, 174109 (2022).

[24] L. Zhang, J. Han, H. Wang, R. Car, and W. E, Deep potential molecular dynamics: A scalable model with the accuracy of quantum mechanics, Phys. Rev. Lett. **120**, 143001 (2018).

[25] J. Behler, Perspective: Machine learning potentials for atomistic simulations, J. Chem. Phys. **145**, 170901 (2016).

[26] L. Zhang, J. Han, H. Wang, W. A. Saidi, R. Car, and E. Weinan, End-to-end symmetry preserving inter-atomic potential energy model for finite and extended systems, in *Proceedings of the 32nd International Conference on Neural Information Processing Systems (NIPS'18)* (Curran Associates Inc., RedHook, 2018), pp. 4441–4451.

[27] Y. Zuo, C. Chen, X. Li, Z. Deng, Y. Chen, J. Behler, G. Csańyi, A. V. Shapeev, A. P. Thompson, M. A. Wood, and S. P. Ong, Performance and cost assessment of machine learning interatomic potentials, J. Phys. Chem. A **124**, 731 (2020).

[28] C. Zhang, L. Tang, Y. Sun, K. M. Ho, R. M. Wentzcovitch, and C. Z. Wang, Deep machine learning potential for atomistic simulation of Fe-Si-O systems under Earth's outer core conditions, Phys. Rev. Mater. **6**, 063802 (2022).

[29] T. Wen, L. Zhang, H. Wang, E. W., and D. J. Srolovitz, Deep potentials for materials science, Mater. Fut. **1**, 022601 (2022).

[30] B. Svendsen and T. J. Ahrens, Shock-induced temperatures of MgO, Geophys. J. Int. **91**, 667 (1987).

[31] G. Kresse and J. Furthmüller, Efficient iterative schemes for ab initio total-energy calculations using a plane-wave basis set, Phys. Rev. B **54**, 11169 (1996).

[32] J. P. Perdew and A. Zunger, Self-interaction correction to density-functional approximations for many-electron systems, Phys. Rev. B **23**, 5048 (1981).

[33] J. P. Perdew, K. Burke, and M. Ernzerhof, Generalized gradient approximation made simple, Phys. Rev. Lett. **77**, 3865 (1996).

[34] J. P. Perdew, A. Ruzsinszky, G. I. Csonka, O. A. Vydrov, G. E. Scuseria, L. A. Constantin, X. Zhou, and K. Burke, Restoring the density-gradient expansion for exchange in solids and surfaces, Phys. Rev. Lett. **100**, 136406 (2008).

[35] P. E. Blöchl, Projector augmented-wave method, Phys. Rev. B **50**, 17953 (1994).

[36] N. A. W. Holzwarth, A. R. Tackett, and G. E. Matthews, A Projector Augmented Wave (PAW) code for electronic structure calculations, Part I: *atompaw* for generating atom-centered functions, Comput. Phys. Commun. **135**, 329 (2001).

[37] Z. Zhang and R. M. Wentzcovitch, Anharmonic thermodynamic properties and phase boundary across the postperovskite transition in $MgSiO_3$, Phys. Rev. B **106**, 054103 (2022).

[38] H. Wang, L. Zhang, J. Han, and W. E, DeePMD-Kit: A deep learning package for many-body potential energy representation and molecular dynamics, Comput. Phys. Commun. **228**, 178 (2018).

[39] J. Zeng, D. Zhang, D. Lu, P. Mo, Z. Li, Y. Chen, M. Rynik, L. Huang, Z. Li, S. Shi *et al.*, DeePMD-Kit v2: A software package for deep potential models, J. Chem. Phys. **159**, 054801 (2023).

[40] D. P. Kingma and J. L. Ba, Adam: A method for stochastic optimization, in *3rd International Conference on Learning Representations* (ICLR, 2015).

[41] Y. Zhang, H. Wang, W. Chen, J. Zeng, L. Zhang, H. Wang, and E. W, DP-GEN: A concurrent learning platform for the generation of reliable deep learning based potential energy models, Comput. Phys. Commun. **253**, 107206 (2020).

[42] F. Mölder, K. P. Jablonski, B. Letcher, M. B. Hall, C. H. Tomkins-Tinch, V. Sochat, J. Forster, S. Lee, S. O. Twardziok, A. Kanitz, A. Wilm, M. Holtgrewe, S. Rahmann, S. Nahnsen, and J. Köster, Sustainable data analysis with snakemake, F1000Research **10**, 33 (2021).

[43] See Supplemental Material at http://link.aps.org/supplemental/10.1103/PhysRevB.109.094101 for the *P-T* ranges covered in AIMD calculations; detailed comparison between this work and other machine-learning potential in describing energy; detailed comparison on elastic coefficients between this work, previous calculations, and previous measurements.

[44] L. Zhang, D. Y. Lin, H. Wang, R. Car, and W. E, Active learning of uniformly accurate interatomic potentials for materials simulation, Phys. Rev. Mater. **3**, 023804 (2019).

[45] A. P. Thompson, H. M. Aktulga, R. Berger, D. S. Bolintineanu, W. M. Brown, P. S. Crozier, P. J. in't Veld, A. Kohlmeyer, S. G. Moore, T. D. Nguyen, R. Shan, M. J. Stevens, J. Tranchida, C. Trotta, and S. J. Plimpton, LAMMPS - a flexible simulation tool for particle-based materials modeling at the atomic, meso, and continuum scales, Comput. Phys. Commun. **271**, 108171 (2022).

[46] S. Nosé, A unified formulation of the constant temperature molecular dynamics methods, J. Chem. Phys. **81**, 511 (1984).

[47] W. G. Hoover, Canonical dynamics: Equilibrium phase-space distributions, Phys. Rev. A **31**, 1695 (1985).

[48] A. Togo and I. Tanaka, First principles phonon calculations in materials science, Scr. Mater. **108**, 1 (2015).

[49] GitHub - abelcarreras/phonolammps: LAMMPS interface for phonon calculations using phonopy, https://github.com/abelcarreras/phonolammps.

[50] M. Parrinello and A. Rahman, Strain fluctuations and elastic constants, J. Chem. Phys. **76**, 2662 (1982).

[51] P. R. C. da Silveira, L. Gunathilake, A. Holiday, D. A. Yuen, M. N. Valdez, and R. M. Wentzcovitch, Ab initio elasticity workflow in the VLab science gateway, in *Proceedings of the Conference on Extreme Science and Engineering Discovery Environment: Gateway to Discovery*, XSEDE '13 (ACM, New York, 2013), pp. 1–8.

[52] C. Luo, J. Tromp, and R. M. Wentzcovitch, Ab initio calculations of third-order elastic coefficients, Phys. Rev. B **106**, 214104 (2022).

[53] M. J. P. Musgrave, *Crystal Acoustics; Introduction to the Study of Elastic Waves and Vibrations in Crystals* (Holden-Day, San Francisco, 1970).

[54] J. Deng, H. Niu, J. Hu, M. Chen, and L. Stixrude, Melting of $MgSiO_3$ determined by machine learning potentials, Phys. Rev. B **107**, 064103 (2023).

[55] F. Yang, Q. Zeng, B. Chen, D. Kang, S. Zhang, J. Wu, X. Yu, and J. Dai, Lattice thermal conductivity of $MgSiO_3$ perovskite and post-perovskite under lower mantle conditions calculated by deep potential molecular dynamics, Chin. Phys. Lett. **39**, 116301 (2022).

[56] G. Fiquet, D. Andrault, A. Dewaele, T. Charpin, M. Kunz, and D. Haüsermann, P-V-T equation of state of $MgSiO_3$ perovskite, Phys. Earth Planet. Inter. **105**, 21 (1998).

[57] G. Fiquet, A. Dewaele, D. Andrault, M. Kunz, and T. Le Bihan, Thermoelastic properties and crystal structure of $MgSiO_3$ perovskite at lower mantle pressure and temperature conditions, Geophys. Res. Lett. **27**, 21 (2000).

[58] Y. Kudoh, E. Ito, and H. Takeda, Effect of pressure on the crystal structure of perovskite-type $MgSiO_3$, Phys. Chem. Miner. **14**, 350 (1987).

[59] S. R. Shieh, T. S. Duffy, A. Kubo, G. Shen, V. B. Prakapenka, N. Sata, K. Hirose, and Y. Ohishi, Equation of state of the postperovskite phase synthesized from a natural (Mg,Fe)SiO_3

orthopyroxene, Proc. Natl. Acad. Sci. USA **103**, 3039 (2006).

[60] W. Utsumi, N. Funamori, T. Yagi, E. Ito, T. Kikegawa, and O. Shimomura, Thermal expansivity of $MgSiO_3$ perovskite under high pressures up to 20 GPa, Geophys. Res. Lett. **22**, 1005 (1995).

[61] N. Funamori, T. Yagi, W. Utsumi, T. Kondo, T. Uchida, and M. Funamori, Thermoelastic properties of $MgSiO_3$ perovskite determined by in situ X ray observations up to 30 GPa and 2000 K, J. Geophys. Res. Solid Earth **101**, 8257 (1996).

[62] L. Stixrude and R. E. Cohen, Stability of orthorhombic $MgSiO_3$ perovskite in the Earth's lower mantle, Nature (London) **364**, 613 (1993).

[63] S. K. Saxena, L. S. Dubrovinsky, F. Tutti, and T. Le Bihan, Equation of state of $MgSiO_3$ with the perovskite structure based on experimental measurement, Am. Mineral. **84**, 226 (1999).

[64] T. Komabayashi, K. Hirose, E. Sugimura, N. Sata, Y. Ohishi, and L. S. Dubrovinsky, Simultaneous volume measurements of post-perovskite and perovskite in $MgSiO_3$ and their thermal equations of state, Earth Planet. Sci. Lett. **265**, 515 (2008).

[65] L. Deng, Z. Gong, and Y. Fei, Direct shock wave loading of $MgSiO_3$ perovskite to lower mantle conditions and its equation of state, Phys. Earth Planet. Inter. **170**, 210 (2008).

[66] B. Wehinger, A. Bosak, S. Nazzareni, D. Antonangeli, A. Mirone, S. L. Chaplot, R. Mittal, E. Ohtani, A. Shatskiy, S. Saxena, S. Ghose, and M. Krisch, Dynamical and elastic properties of $MgSiO_3$ perovskite (Bridgmanite), Geophys. Res. Lett. **43**, 2568 (2016).

[67] G. F. Davies, Effective elastic moduli under hydrostatic stress—I. Quasi-harmonic theory, J. Phys. Chem. Solids **35**, 1513 (1974).

[68] Z. Wu and R. M. Wentzcovitch, Quasiharmonic thermal elasticity of crystals: An analytical approach, Phys. Rev. B **83**, 184115 (2011).

[69] J. P. Watt, Hashin-Shtrikman bounds on the effective elastic moduli of polycrystals with orthorhombic symmetry, J. Appl. Phys. **50**, 6290 (1979).

[70] R. Hill, The elastic behaviour of a crystalline aggregate, Proc. Phys. Soc. Sect. A **65**, 349 (1952).

[71] A. M. Dziewonski and D. L. Anderson, Preliminary reference earth model, Phys. Earth Planet. Inter. **25**, 297 (1981).

[72] R. M. Wentzcovitch, B. B. Karki, S. Karato, and C. R. S. Da Silva, High pressure elastic anisotropy of $MgSiO_3$ perovskite and geophysical implications, Earth Planet. Sci. Lett. **164**, 371 (1998).

[73] F. D. Stacey and P. M. Davis, *Physics of the Earth* (Cambridge University Press, Cambridge, 2008), 4th ed.

[74] J. J. Valencia-Cardona, G. Shukla, Z. Wu, C. Houser, D. A. Yuen, and R. M. Wentzcovitch, Influence of the iron spin crossover in ferropericlase on the lower mantle geotherm, Geophys. Res. Lett. **44**, 4863 (2017).